Materials Chemistry and Physics 263 (2021) 124366

Contents lists available at ScienceDirect

Materials Chemistry and Physics

journal homepage: www.elsevier.com/locate/matchemphys

Optimization of the morphology, structure and properties of high iron content Zn–Fe coatings by pulse electrodeposition

C. Arrighi [a,b], C. Savall [a], S. Cohendoz [a], J.-L. Grosseau-Poussard [a], L. Baissac [c], M.-G. Olivier [b,d], J. Creus [a,*]

[a] Laboratoire des Sciences de l'Ingénieur pour l'Environnement (LaSIE) UMR CNRS 7356 – La Rochelle University, Av. Michel Crépeau, 17042, La Rochelle, France
[b] University of Mons-UMONS, Faculty of Engineering, Materials Science Department, Place du Parc, 20, 7000, Mons, Belgium
[c] IRT M2P, 12 Rue de l'Artisanat, 67120, Duppigheim, France
[d] Materia Nova ASBL, Avenue Copernic 1, 7000, Mons, Belgium

HIGHLIGHTS

- Improvement of the morphology of high iron content Zn–Fe alloys using pulse electroplating.
- Incorporation of iron increase the hardness of the coatings but affecting its adhesion.
- Ennoblement of the corrosion potential with iron incorporation.

ARTICLE INFO

Keywords:
Electrodeposition
Zinc-iron
Coating
Pulse current

ABSTRACT

An additive-free gluconate based alkaline electrolyte was used to study the electrodeposition of Zn and Zn–Fe coatings. Cyclic voltammetry was performed to define the accurate deposition parameters and to identify the reactions taking place. Electrodeposition was performed using direct and pulse currents. Electrodeposits were characterized in terms of morphology, microstructure, mechanical and corrosion properties. Homogeneous Zn and Zn–Fe 7 wt% Fe were obtained, composed of hexagonal and blunted pyramidal grains respectively. Pulse current deposition was carried out to improve the morphology and to reduce the impact of hydrogen evolution reaction. Deposition parameters such as on-time/off-time/peak current density ($t_{on}/t_{off}/j_p$) were investigated. The average current density j_m seems to control the composition of Zn–Fe electrodeposits. High iron contents were obtained at low current densities and the iron content abruptly decreased when the current density increased for both direct and pulse currents electrodeposition. Incorporation of iron led to an increase of the micro-hardness of the coating. Scratch tests were performed in order to evaluate the damage of the coatings, and the coating adhesion could be assessed. Polarization curves in 3.5 wt% NaCl after 1 h of immersion at the open circuit potential did not show any change of corrosion potential between Zn and Zn–Fe 7 wt% Fe deposits. This potential was shifted to a more positive value for Zn–Fe 14 wt% Fe, which points out this coating as the best choice to reduce the galvanic corrosion between the steel substrate and the Zn–Fe deposit. These results were linked to the microstructure of the deposits and perhaps to the presence of Γ_1-Fe_5Zn_{21} phase for Zn–Fe 14 wt% Fe.

1. Introduction

Electrodeposited cadmium coatings have been widely used for many years as sacrificial coatings for steel substrates in the industry. However, due to the toxicity of cadmium, European regulations have tried to limit their use encouraging the development of alternative solutions [1]. Electrodeposited zinc-based coatings were investigated at the beginning of the 90's. Several works have shown that alloying zinc with an iron-group metal (Ni, Co or Fe) improves their corrosion resistance by reducing the potential difference compared with steel substrate [2,3]. Among them, Zn–Ni electrodeposited coatings with 12–14 wt% of Ni were particularly investigated because of their improved performance

* Corresponding author.
E-mail address: juan.creus@univ-lr.fr (J. Creus).

https://doi.org/10.1016/j.matchemphys.2021.124366
Received 19 December 2020; Received in revised form 1 February 2021; Accepted 6 February 2021
Available online 8 February 2021

[4–6]. Recent concerns about the toxicity of nickel and cobalt salts have encouraged studies to propose more eco-friendly alternatives, such as Zn–Fe coatings.

Several electrolytes were proposed in the literature to obtain Zn–Fe deposits: acidic or alkaline formulations, with sulfate [7–15], chloride [16–20] or both salts [21–24]. Few studies were based on the use of zincate baths [25–29], which have shown to be more efficient in terms of throwing power. Additives are often used to improve the properties of the coatings (covering, brightness). Such a diversity of electrolytic baths allows to obtain Zn–Fe deposits whose iron composition varies from 0 to about 100 wt% but the literature is mainly devoted on low iron contents.

Zn–Fe deposition is often reported as anomalous [7,17,19,28,30]. In such case, zinc which is the less noble metal will be preferentially deposited. This kind of deposition mode has also been reported for Zn–Ni and Zn–Co systems [30–32]. Although only few assumptions were proposed yet to explain this phenomenon, it seems that a transition between anomalous and normal codeposition can be observed in the same electrolytic bath with the variation of the applied current density [28,30,33,34]. Due to the anomalous codeposition mechanism, many studies deal with alloys containing less than 10 wt% of iron [15,17,18, 21,23,25–27].

Recently, the use of simple pulse plating (SPP) has been investigated to improve the morphology and performance of electrodeposits. Many advantages can be attributed to the use of pulse current (PC): decrease of the grain size [17,21,26,35–39], porosity rate reduction [17,35] and better homogeneity [17,36]. Reverse pulse plating (RPP) can be used to reduce the roughness of deposits and also to change the composition of the coatings [21,26,35,37,38]. Concerning the electrodeposited Zn–Fe deposits, very few studies are dealing with the impact of pulse plating on the characteristics and/or properties of the coatings [17,21,26,40]. The variation of the electric parameters (such as duty cycle, pulse peak current density and frequency) permits to modify the iron content up to 1.5 wt % in acidic baths [17] or less than 1 wt% in alkaline baths [21, 26]. Ge et al. [40] reach a maximum iron content value of 6–7.4 wt% and they underline that pulse current permits to modify the texture and phase composition of Zn–Fe coatings deposited from an alkaline bath. Finally, pulse plating (like SPP or RPP) has never been studied in the case of high iron amount in Zn–Fe systems and it could be an interesting way to improve the morphology and corrosion properties of these sacrificial coatings.

According to the equilibrium diagram [41], the solubility limit of iron in the HCP η-Zn phase is very low, lower than 0.03 wt%. Different phases can be obtained according to the Fe content:ζ-$FeZn_{13}$ (5–6 wt% Fe), δ-$FeZn_{10}$ (7–11.5 wt% Fe), Γ_1-Fe_5Zn_{21} (17–19.5 wt% Fe), Γ-Fe_3Zn_{10} (23.5–28 wt% Fe) and α-Fe solid solution. Based on the literature, a link can be established between the structure of electrodeposits obtained in acidic electrolytes and their iron content [8,9,11,13,16,18,22,23,42, 43]. For low iron contents, η is the main crystallographic phase, with small amounts of δ. The amount of η decreases with the increase of the iron content, associated to the increase of δ and/or Γ_1/Γ.

The presence of some crystallographic phases can be crucial regarding the functional properties of the coatings. Indeed, the good corrosion resistance of Zn–Ni coatings with 12–14 wt% Ni is attributed to the presence of the single γ-Ni_5Zn_{21} crystallographic phase [4]. The same crystallographic phase is present in the Zn–Fe diagram: Γ_1-Fe_5Zn_{21}. Increasing the iron content of Zn–Fe deposits up to 15 or 20 wt% Fe should lead to the presence of such phase, thus maybe increasing their anti-corrosion properties.

Since Zn–Fe is mainly used as a sacrificial coating, very few information was found regarding its mechanical properties [9–11]. They all concluded that the addition of iron increased the hardness of the coating, from 56 HV for pure zinc to 203 HV for Zn–Fe 14 wt% Fe, leading to a loss of ductility. Panagopoulos et al. [10] conducted sliding wear behaviour tests on zinc-based electrodeposits. The main wear mechanism was found to be plastic deformation for coatings containing up to 6 wt% of iron. When the iron content increased to 14 wt%, this mechanism became less intense.

During the 90's, authors claimed that only a small amount of iron or cobalt was required to improve the corrosion resistance of zinc electrodeposits and that higher iron contents could lead to a performance decrease due to the presence of brittle zinc-iron phases. Authors mentioned a significant improvement of corrosion properties with such low iron contents, compared with zinc [3,44]. Recently, the impact of higher iron contents (up to about 30 wt%) on the corrosion resistance of Zn–Fe electrodeposits was investigated. Regarding the impact of the iron content, contradictory results were obtained, probably due to differences in metallurgical states of the Zn–Fe coatings deposited from acidic or alkaline baths with or without additives. Lan et al. [29] and Park et al. [12] noticed an ennoblement of the corrosion potential with the increase of the iron content while Nayana et al. [13] observed a reverse tendency. On the other hand, Bhat et al. [45] highlighted an increase followed by a decrease of the corrosion potential with the increase of the iron content (from 2.1 to 6.8 wt% Fe). Furthermore, no clear influence of the iron content was observed on the corrosion current density. The comprehension of the corrosion resistance of high iron content Zn–Fe coatings is still unclear, and it requires to be correlated with the metallurgical structure and defects.

This study aims at understanding the relationship between the metallurgical state of the Zn–Fe deposits (composition, structure) and their corrosion resistance. An additive-free alkaline electrolyte was used in order to avoid the incorporation of organic pollutants. Zn and Zn–Fe coatings with several iron contents (max 20 wt%) were deposited by modifying the electrolyte composition and the deposition parameters. The objective was to obtain deposits with different microstructures, and particularly to define whether it was possible to obtain a single-phase Γ_1-Zn-Fe coating in order to evaluate its corrosion behaviour. Since the impact of pulse current has scarcely been investigated for alloys containing more than 5 wt% Fe, the influence of pulse parameters was assessed in terms of morphology, microstructure, and iron content. Pulse current deposition was used to obtain the accurate morphology with the fewer defects in order to avoid additives in the electrolyte. Many studies focused on the corrosion resistance of rather low iron content deposits in relation with the structure and morphology. But very few of them investigated the mechanical behaviour of Zn–Fe films. However, all these parameters have scarcely been correlated, particularly using pulse current. Consequently, this study will focus on the influence of the electrical parameters (current density and pulse conditions) on the iron content, the morphology and the microstructure of Zn–Fe coatings in relation with their electrochemical and mechanical properties.

2. Experimental

All electrolytes were prepared by dissolving chemical grade reagents in ultrapure water. An additive-free electrolyte proposed by Lan et al. was used [29]. This electrolyte is composed of potassium hydroxide (KOH, from Sigma Aldrich), zinc oxide (ZnO, from Merck) and ferrous gluconate ($C_{12}H_{22}FeO_{14}{\cdot}2H_2O$, from Sigma Aldrich). The electrolyte pH was superior to 14 due to the high amount of potassium hydroxide. Such alkalinity is required to solubilize zinc oxide and to provide zincate ions. The use of ferrous gluconate avoids the addition of other complexing agents. Four different electrolytes were prepared as presented in Table 1, in order to understand the role of each component and its impact regarding electrochemical reactions.

A conventional three-electrode cell composed of a Pt-coated titanium counter electrode, a Saturated Calomel Electrode (SCE) as the reference electrode inserted in a Luggin capillary filled with saturated KCl (from VWR Chemicals) solution, and finally the working electrode composed of AISI 4337 steel or pure copper. A 500 mL double jacket cell equipped with a cryostat was used to control the temperature of the bath at 25 ± 1 °C. The electrolyte was magnetically stirred at 350 rpm.

Two substrates were used: 99.5% copper (Ø 15 mm) and AISI 4337 steel barrel (Ø 20 mm). The composition of the steel is presented in

Table 1
Composition of the electrolytes used for the study.

Electrolyte	[KOH] (mol/L)	[ZnO] (mol/L)	[$C_{12}H_{22}FeO_{14}\cdot 2H_2O$] (mol/L)	Fe/Zn (molar ratio)
KOH (bath 1)	6.6	0	0	0
Zn (bath 2)	6.6	0.3	0	0
High iron content (bath 3)	6.6	0.3	0.075	0.25
Low iron content (bath 4)	6.6	0.5	0.0125	0.025

Table 2.

Metallic substrates were cut into 2 mm thick samples and enrobed in epoxy resin (Presi Mecaprex). They were then ground with silicon carbide until 4000 grade and rinsed with ultrapure water and in absolute ethanol in an ultrasonic bath.

Voltammograms and deposits were obtained with a VSP Biologic potentiostat equipped with a 4 A booster. Cyclic voltammetry was performed in the different electrolytes between −1 V/SCE and −2 V/SCE at 20 mV/s. This technique allows to determine the optimal deposition parameters and to identify the cathodic and anodic reactions that occur versus the electrolyte composition.

Deposition times were adjusted in order to obtain a 15 μm thick deposit. After deposition, the samples were rinsed with ultra-pure water and dried. The weight of the samples was measured before and after deposition to calculate the cathodic current efficiency (CCE) using the following equation:

$$CCE = \frac{w_{exp}}{w_{th}}.100 \quad (1)$$

w_{exp} is the experimental coating weight measured after deposition and w_{th} is the theoretical coating weight deduced from the Faraday's law considering the iron alloy composition:

$$w_{th} = \frac{jSt.10^{-3}}{F}\left(\frac{x_{Fe}}{n_{Fe}}.M_{Fe} + \frac{x_{Zn}}{n_{Zn}}.M_{Zn}\right) \quad (2)$$

where j is the applied current density, S is the sample surface, t is the deposition time, F is the Faraday constant (96485 C/mol), x_x is the atomic ratio of the element x in the alloy, n_x is the number of exchanged electrons during the reduction reaction, and M_x is the molar mass of the element x.

Coatings were first deposited using potentiostatic methods to evaluate the relationship between the deposition potential and the iron content. Galvanostatic deposition method was then used to control the thickness of the deposits. The influence of deposition parameters was investigated using direct current (DC) and pulse current (PC) methods. Several parameters must be taken into account for PC experiments: the on-time (t_{on}), the peak current density (j_p), the off-time (t_{off}), the average current density (j_m), the duty cycle (γ) and the frequency (f) [35].

The average current density can be calculated with the following formula:

$$j_m = \frac{j_p.t_{on}}{t_{on} + t_{off}} = j_p.\gamma \quad (3)$$

The characterization of the deposits was carried out following a multi-scale approach. The chemical composition was determined by μ X-Ray Fluorescence (μ XRF) using a Bruker M4 Tornado with a Rhodium source operating at 35 kV and 160 μA under a pressure of 20 mbar for the deposits on copper substrates. Energy Dispersive Spectroscopy (EDS) was performed on the deposits applied on steel substrates on 3.4 mm^2 areas. The surface morphology of the films was observed with a Field Emission Gun Environmental Scanning Electron Microscope (FEG ESEM) Philipps Quanta 200 at 20 kV. Secondary Electron (SE) images were displayed to highlight the topography of the alloys. The cross-section of the samples was also analysed by SEM after two different sample preparations. For the first one, the coated samples were cut through a Struers Secotom precision cutting machine equipped with a diamond cut-off wheel. The obtained cross-sections were then ground using silicon carbide paper until 4000 grade, and a final diamond paste polishing was performed with ethanol to avoid the degradation of the zinc-based coating. The second method consisted of cryogenic fractures in liquid nitrogen of a pre-notched coated sample.

The polished cross-sections were used to evaluate the thickness heterogeneities and to measure more accurately the coating thickness while the cryofractures give more information on the morphology and the growth mechanism of the deposits. Finally, the crystallographic phases of the coatings were determined using X-Ray Diffraction (XRD) thanks to a Bruker AXS D8-Advanced device. Diffractograms were registered from 33 to 100° with Cu-Kα radiation (λ = 0.15406 nm) with a step size of 0.01°.

A micro-indentation instrument (Anton Paar MCT^3 STEP 4) equipped with a diamond Vickers indenter was used to evaluate the mechanical properties of the coatings. In order to minimize the substrate effect and to ensure the reliability of the data, the normal load was optimized in order to limit the penetration depth to approximately 2 μm [46]. Five micro-indentations were made on each coating with a constant load of 10 g. The normal load was applied by a progressive charging of 200 mN/min during 30 s and a constant load for 5 s. The obtained stamps were examined by means of an optical microscope in order to estimate the average diagonal magnitude. Microhardness calculations were carried out according to Ref. [47]:

$$H = 1854.\ \frac{P}{d^2} \quad (4)$$

where: H is the microhardness, P is the applied mechanical load (g), and d is the average diagonal magnitude (μm) of the indention stamp.

Scratch test was used to evaluate the adhesion of the coating to the substrate. Even if the scratch test does not directly give information about the adhesion of the coating, test parameters and coating thicknesses were quite similar, permitting a comparison of the adhesion of the different coatings. The experiments were performed thanks to an Anton Paar MCT^3 STEP 4 equipment with an indenter corresponding to a Rockwell sphero-conical diamond tip with 90° angle and 50 μm radius. The indenter speed was fixed at V = 8 mm/min on 4 mm length tracks and measurements were performed at room temperature and repeated at least four times, with a distance of 1 mm between each scratch. Vertical loading mode was used and a linearly increasing load F_z from 0.01 N up to 5 N was applied on the total track length. In order to compare and characterize the adhesion of the electrodeposited coatings onto steel substrate, the coating thickness was fixed at around 10 μm for the micro-indentations and scratch tests.

For the corrosion resistance assessment, a conventional three-electrode cell was used, composed of a Pt grid as the counter electrode, a Saturated Calomel Electrode (SCE) as the reference electrode inserted in a Luggin capillary filled with saturated KCl solution, and finally the working electrode composed of steel, Zn or Zn–Fe coated

Table 2
Composition of the AISI 4337 steel.

Element	C	S	Mo	Cr	Ni	Mn	P	Si
Wt. %	0.32–0.39	<0.035	0.25–0.45	1.60–2.00	3.60–4.10	0.30–0.60	<0.035	0.10–0.40

steel. The exposed surface was delimited to 1 cm^2 with the use of Lacomit varnish. A 500 mL double jacket cell equipped with a cryostat was used to control the temperature of the bath at 25 ± 1 °C. The electrolyte was magnetically stirred at 250 rpm. Tests were carried out in aerated 3.5 wt% NaCl (from VWR Chemicals) solution adjusted to pH 7 with 0.01 M NaOH (from Sigma Aldrich) solution. A Solartron Modulab potentiostat was used to carry out corrosion tests that consisted in two steps: 1 h of immersion at the Open Circuit Potential (OCP) followed by a Linear Sweep Voltammetry from −0.15 V/OCP to 0.2 V/OCP at a scanning rate of 0.2 mV/s. Otherwise, the experiment stopped when the current density reached 7.10^{-4} A/cm^2.

3. Results and discussion

3.1. Electrochemical behaviour of the electrode in the deposition bath

Fig. 1 displays the cyclic voltammograms obtained on copper substrate in baths 1, 2 and 3 described in Table 3. The variation of the bath composition is helpful for the study of the electrochemical reactions occurring at the metal/electrolyte interface during the polarization.

Fig. 1 (a) presents the comparison of the cyclic voltammograms obtained on copper substrates in baths 1 and 2. Bath 1 is composed of potassium hydroxide, so during the cathodic polarization, it is obvious that only two reduction reactions could be observed. The first one is associated to a large plateau representing the reduction of dioxygen. The second one becomes noticeable for potentials more negative than −1.6 V/SCE. The increase of current density is due to the water reduction, causing the dihydrogen evolution on the working electrode. This reaction also produces hydroxide ions OH^-, according to the following reaction in alkaline medium:

$$2\,H_2O + 2\,e^- \rightarrow H_{2\,(g)} + 2\,OH^-$$

The potential associated to this reaction can be calculated from the Nernst equation. Assuming the activity coefficient of OH^- ions to be equal 1, the equilibrium potential would be close to −1.12 V/SCE. An overpotential of about 0.48 V can be associated to this reaction. The overpotential of Hydrogen Evolution Reaction (HER) depends on different parameters such as the electrolyte composition and pH, the bath temperature and the nature of the cathode [48].

In bath 2, where zinc oxide is added, the reduction reaction of dioxygen is also observed at the beginning of the cathodic polarization. The current density began to decrease at −1.58 V/SCE. This reduction peak was associated to the formation of a Zn film. Since we used a zincate electrolyte, the reduction reaction that took place on the substrate is:

$$ZnO_2^{2-} + 2\,e^- + 2\,H_2O \rightarrow Zn_{(s)} + 4\,OH^-$$

The potential associated to the reduction of zincate ions was calculated with the formula proposed by Nakano et al. [28]. We assumed the activity coefficients of OH^- and ZnO_2^{2-} ions to be equal 1. Because of the consumption of 2 mol of OH^- to form one mol of ZnO_2^{2-} from solid ZnO particles, the activities of OH^- and ZnO_2^{2-} could respectively be approximated to 6 and 0.3. Consequently, the calculated equilibrium potential is −1.56 V/SCE, which is in very good agreement with the experimental value deduced from the voltammogram.

During the deposition process, the region in contact with the electrode surface is depleted in metallic ions. Diffusion phenomenon replenishes the vicinity of the electrode in metallic species. The voltammogram presents a limiting current density at 60 mA/cm^2 due to diffusion limitation. Consequently, it was decided to limit the applied current density in DC mode to 50 mA/cm^2 for Zn deposits in order to avoid the formation of dendritic deposits. Finally, the presence of zinc on the electrode shifted the HER towards a more negative potential (−1.9 V/SCE) due to a higher overpotential of HER on Zn than on copper. In this electrolyte, the equilibrium potential associated to HER is −1.12 V/SCE, so there is an overpotential of 0.78 V.

In the anodic part (j > 0), the oxidation of the Zn coating deposited during the cathodic potential sweep begins at −1.57 V/SCE that is close to the equilibrium potential of the zincate/zinc couple. The complete dissolution of the film is observed.

When ferrous gluconate is added into the electrolytic bath, two reduction processes are observed respectively at around −1.45 V/SCE and −1.62 V/SCE (Fig. 1 (b)). It seems that the latter one perfectly matches with the zincate reduction peak previously described for the bath 2 and should correspond to the formation of a quite zinc rich phase. Thus, the reduction peak observed at −1.45 V/SCE is attributed to the formation of iron rich phases. For high cathodic potential at around −1.8 V/SCE, a large increase of the current density is associated to HER that occurs on zinc-iron phases. The presence of iron in the deposit decreases the overpotential associated to the HER from 0.79 V to 0.69 V and increases the associated current density. The diffusional limiting current density is slightly lower, with a value of 40 mA/cm^2 that reduces the range of applied current densities for the electrodeposition of Zn–Fe coatings in DC mode. Regarding the HER, Fig. 1 reveals the influence of the nature of the substrate on the overpotential values for the rise of the current density: copper favours more this reaction than zinc-iron which promotes it more than zinc.

During the reverse potential sweep, the oxidation of the Zn–Fe coatings occurs at a more positive potential, at around −1.43 V/SCE. due to the iron incorporation. The area of the dissolution peak is smaller, suggesting that less metallic ions were reduced during the cathodic sweep, which is consistent with the increase of the water reduction kinetics. It was also noticed that the current density did not return to zero at the end of the experiment, suggesting the presence of iron rich phases that should be dissolved at higher anodic potential. This point was confirmed by the presence of a metallic layer still visible on the copper

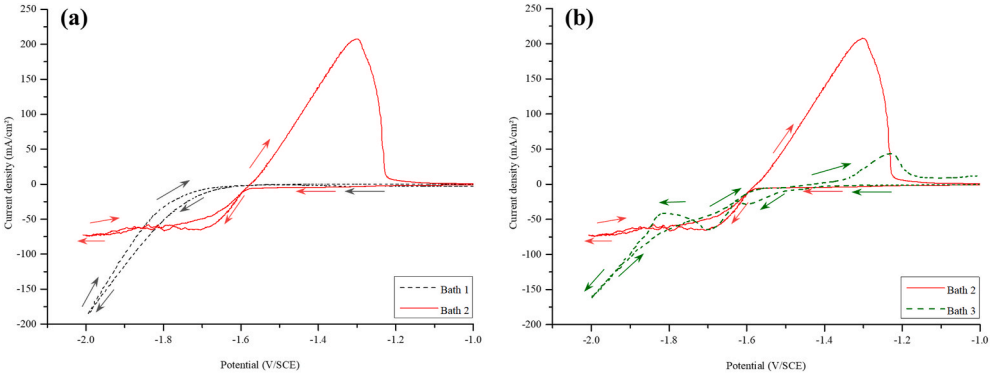

Fig. 1. Cyclic voltammograms for bath 1 and bath 2 (a), and bath 2 and bath 3 (b) on copper substrates with a scan rate of 20 mV/s at 25 °C under magnetic stirring (350 rpm).

Table 3
Elaboration conditions, iron content and deposition potential of PC deposits, with j_m 25 mA/cm^2 at 25 °C in bath 3 under magnetic stirring (350 rpm).

Sample	t_{on} (ms)	t_{off} (ms)	j_p (mA/cm^2)	j_m (mA/cm^2)	%Fe	$E_{deposit}$ (V/SCE)
Zn-Fejp75	4	8	75	25	15.3	−1.72
Zn-Fejp125	4	16	125	25	14.5	−1.80
Zn-Fejp175	4	24	175	25	15.5	−1.83
Zn-Fejp225	2	16	225	25	15.5	−1.96
Zn-Fejp1025	0.4	16	1025	25	16.3	−3.20

substrate at the end of the experiment. Some authors have attributed the anodic peak to the dissolution of Zn from the η phase [7,18]. Consequently, the remaining metallic layer would be composed of iron rich and/or Zn from other phases.

In order to confirm the cathodic reactions occurring at the surface of the copper substrate, potentiostatic experiments were carried out at different potential values: 1.45, −1.57 and −1.62 V/SCE for 5 min. μ-XRF analyses were performed in order to evaluate the composition of the coatings. The coatings obtained at −1.45, −1.57 and −1.62 V/SCE are respectively composed of 82, 24 and 15 wt% of iron, highlighting a decrease of the iron content with the deposition potential. Consequently, as expected, the first reduction peak is mainly attributed to the formation of iron rich phases and the second one to the formation of zinc rich phases. However, it seems that the reduction of zinc starts at a potential nobler than −1.57 V/SCE in the Zn–Fe electrolyte. Such underpotential deposition (UPD) of zinc has already been mentioned in the literature by Nakano et al. for zincate Zn-Fe [28], Zn-Ni [33] and Zn–Co [34] systems.

3.2. Formation of Zn and Zn–Fe deposits by DC mode

As mentioned in the experimental section, all the coatings were deposited in a galvanostatic mode to obtain 15 μm thick deposits. A preliminary study performed on copper substrates was carried out in bath 3 in order to identify the limiting conditions and to determine the accurate deposition parameters. μ-XRF measurements were performed to evaluate the composition of the Zn based coatings.

As expected from the voltammetric study, the deposit obtained at 10 mA/cm^2 was mainly composed of iron (about 90 wt%). An increase of the current density (25 mA/cm^2) led to a large decrease of the iron content (14 wt %). But a further increase of the current density in the range of 40–60 mA/cm^2 resulted in dendritic deposits, which is consistent with the limiting current density highlighted by the cyclic voltammogram. Since 14 wt% Fe was in the range of our objective, it was decided to perform the galvanostatic deposits at 25 mA/cm^2.

Two coatings were deposited by DC on steel substrates: zinc coating (Zn) from electrolyte 2 and zinc-iron coating with 14 wt% Fe (ZnFe14) from electrolyte 3. For these coatings, no major impurity was detected by EDS and the amount of oxygen was inferior to 1 wt%. The CCE was

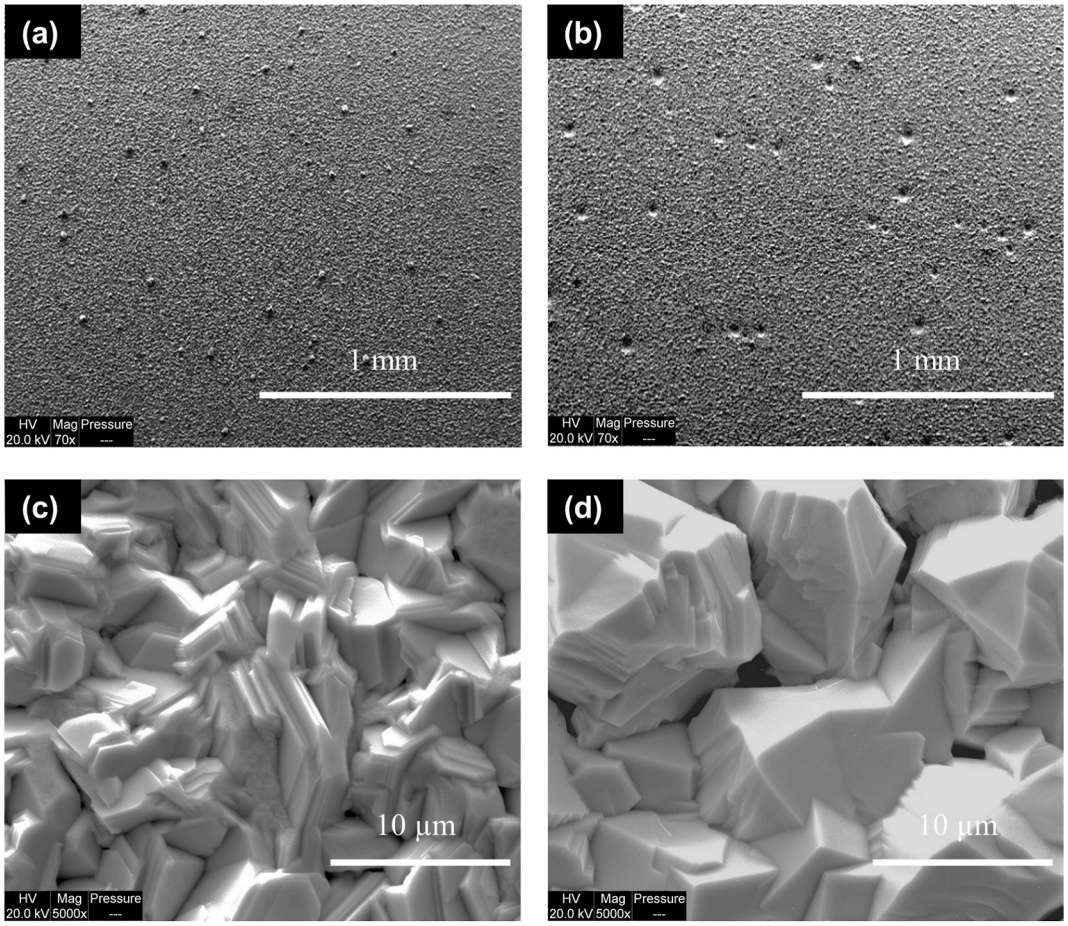

Fig. 2. SEM images (SE) of the surface of DC electrodeposits obtained at 25 mA/cm^2: Zn (a, c), and ZnFe14 (b, d).

between 80 and 90% for Zn and superior to 90% for ZnFe14. The morphology of these deposits will first be presented, and the microstructure of the coatings will be discussed later.

Fig. 2 presents surface SEM observations of the Zn-based electrodeposited coatings. Electrodeposited Zn coating presents a homogeneous morphology with the presence of few aggregates that are spread all over the surface as presented in Fig. 2 (a). EDS analyses on these aggregates did not show any composition differences (such as the oxygen content) with the other parts of the deposit. High magnification views reveal that the zinc coating is composed of typical packets of hexagonal platelets with various orientations as described in a previous work [49].

When iron is incorporated into the zinc deposit, the formation of numerous pores can be observed on the surface of ZnFe14 in Fig. 2 (b). The presence of these pores is probably due to the water reduction and the hydrogen evolution that is promoted by the iron incorporation. The pores are randomly distributed on the whole surface of the electrode with diameters varying from 15 to 73 μm. High magnification views reveal that the Zn–Fe coating presents a pyramidal morphology with faceted surfaces and larger crystallites compared to pure zinc coating.

Fig. 3 presents the SEM cross section of the Zn–Fe coatings. Surface roughness is quite high due to the coarse Zn–Fe grains and the average thickness is close to 15 μm. The pores could lead to local reduction of the thickness of the coating and in some case to the absence of coating as showed in SEM analysis of ZnFe14 cross-section. The pore diameters measured on cross-sections (around 36 μm) were in good agreement with the ones measured on the SEM surface images.

The change from hexagonal to pyramidal grains with the increase of the iron content has already been reported in the literature [8,14,50]. This evolution is attributed to the microstructure of the alloys and particularly to the change of crystallographic phases.

The presence of numerous pores on the surface of ZnFe14 that could reduce the anticorrosion properties, led to consider the use of pulse current to improve the coating morphology.

3.3. Improvement of the coating morphology: PC deposition

Pulse current was applied on steel substrates in order to improve the morphology of ZnFe14 coating by using the bath 3. First, the influence of the pulse parameters was investigated with electrodeposits performed at the same average current density j_m as for ZnFe14, *i.e.* 25 mA/cm^2. For all the PC deposits, the CCE was superior to 90% and the amount of oxygen detected by EDS was inferior to 1.5 wt%.

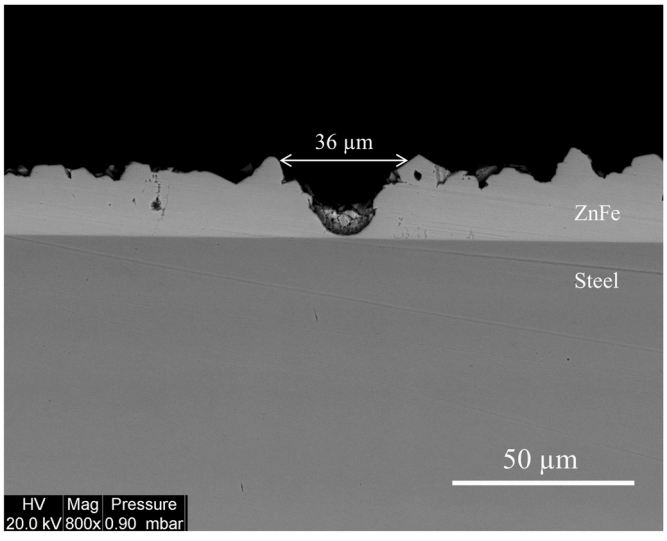

Fig. 3. SEM image (BSE) of the cross-section of ZnFe14 with the presence of pores.

The use of PC deposition contributes to the replenishment of the diffusion layer, so it is possible to apply higher cathodic current densities during the on-time compared to DC deposition. Different conditions were investigated, as listed in Table 3. The influence of two couples of parameters was investigated: t_{on}/j_p and t_{off}/j_p. Indeed, the adjustment of j_p was necessary with the change of t_{on} or t_{off} to maintain a constant value of j_m.

It can be noticed that for all deposits elaborated with j_m = 25 mA/cm^2, the iron content was in the same range that the one obtained by DC (14.9 ± 1.1 wt% Fe). Despite the large variation of j_p, t_{on} and t_{off} parameters, no significant change in the composition was observed. This observation can be used to discuss the evolution of the deposits considering pulse parameters exclusively and to exclude the contribution of a change of the iron content. Despite the variations of pulse parameters such as t_{on}, t_{off} and j_p, the iron contents are quite similar to those detected in DC mode for the same values of j_m. This suggests that the current density j_m mainly controls the iron contents in the Zn–Fe alloys [39,51]. Similar observations were reported by Pagotto et al. [39] for Zn–Ni coatings deposited by DC and PC modes at the same average current density of 50 mA/cm^2.

3.3.1. Reduction of the pores number

Previous results showed the presence of numerous pores on the surface of ZnFe14. The use of PC and particularly the modification of t_{off} should favour the desorption of hydrogen on the cathode surface and the replenishment of the diffusion layer, thus should limit the number of pores. Fig. 4 displays low magnification SEM images for different pulse conditions. The first evidence is the evolution of the pore density on the coating surface when deposition parameters are changed.

When t_{on} decreased, the number of pores increased. As explained previously, j_p increased as t_{on} decreased, leading to more negative deposition potentials (Table 3). In part 3.1, the cyclic voltammograms highlighted an increase of the HER with decreasing the cathodic potentials. Since these deposits were obtained at the same t_{off}, namely 16 ms, it can be supposed that for the highest j_p, this value was not sufficient to permit the desorption of the hydrogen adatoms produced during the deposition pulse.

Fig. 4 shows, that for the same t_{on} value of 4 ms, the pores number first decreases and then increases as t_{off} and j_p increase. As previously mentioned, it can be expected that the longer the off-time, the lesser the number of pores. However, an increase of the off-time was also associated to higher pulse current density j_p and more negative deposition potentials. Thus, longer off-times induce more hydrogen produced and so the presence of a high density of pores.

These two opposite effects are quite visible on SEM images (Fig. 4). First, 8 ms of off-time was too short to avoid the formation of pores in comparison with DC coating. When t_{off} increased to 16 ms, a quite homogeneous surface with very few pores was obtained, but a further increase of t_{off} at 24 ms, coupled to the highest value of the cathodic current density leads to an increase of the number of pores.

These results showed that PC deposition can lead to an improvement of the coatings with a reduction of the pores number, but an optimized set of parameters $t_{on}/t_{off}/j_p$ has to be defined. In that case, the set 4 ms/16 ms/125 mA/cm^2 seemed efficient.

3.3.2. Refinement of the microstructure

High magnification SEM images (Fig. 5) highlight the morphology of the deposits and the influence of pulse parameters (t_{on}, t_{off} and j_p) on the refinement of the microstructure.

The coatings deposited by PC present a pyramidal morphology quite similar to the coating deposited by DC, probably due to the fact that the iron content is close for all these coatings.

The first observation is that all PC deposits present finer morphologies than the DC one. Such effect is commonly observed in the literature [17,21,26,35–39]. The nucleation rate determines the number of nuclei formed. It is related to the overpotential with the following

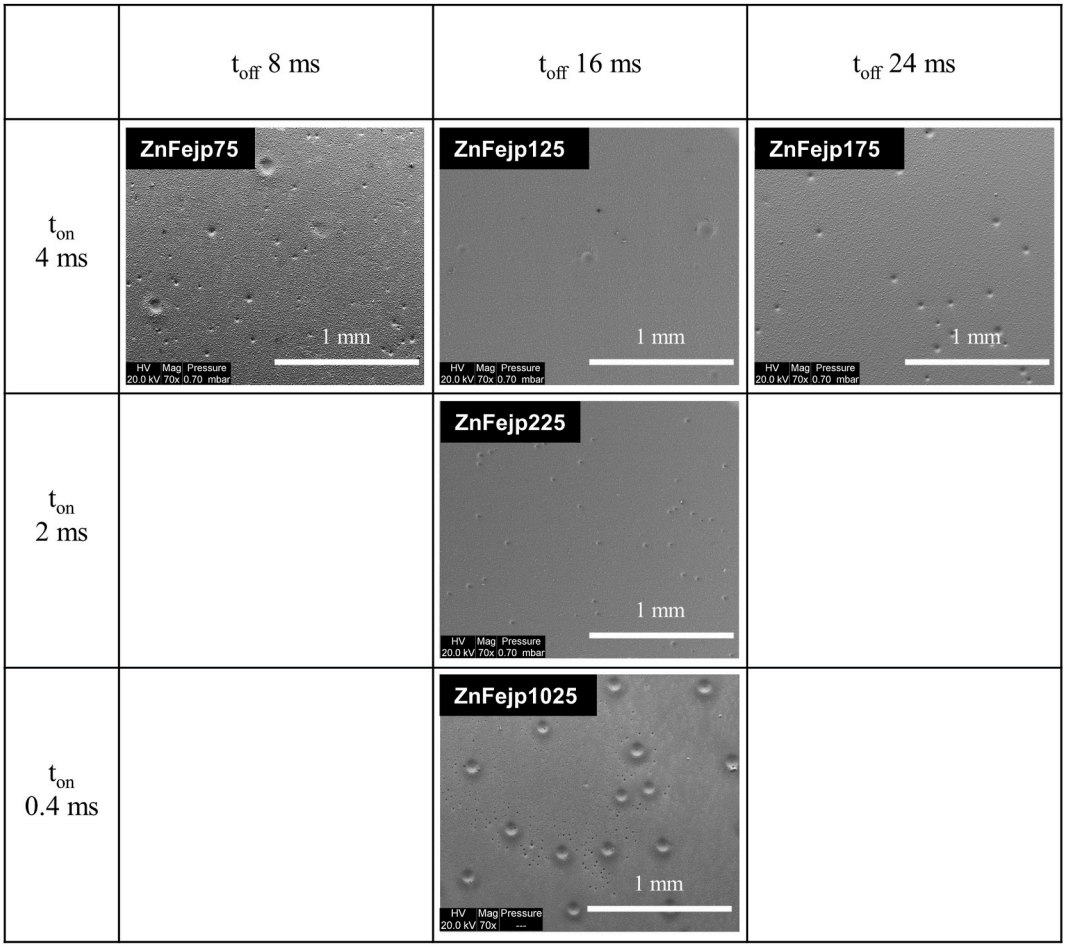

Fig. 4. SEM images (SE) at low magnification (x70) of the surface of PC deposits obtained at j_m 25 mA/cm^2 on steel substrates, in function of the off-time and the on-time. The pulse current density is given with the name of each specimen.

equation [35]:

$$\nu = K_1 \, e^{\frac{-K_2}{|\eta|}}$$

Where K_1 is proportionality constant, K_2 is the amount of energy needed for nucleation and η is the overpotential.

The refinement of the microstructure is mainly visible between ZnFe14 and ZnFejp75, which have a difference of 70 mV regarding deposition potentials (Table 3). However, no difference is measured between ZnFejp75 and ZnFejp125 even though ZnFejp125 has a deposition potential 80 mV lower than ZnFejp75 (Table 3). This observation suggests that the overpotential differences may not be enough due to the contrary effects of t_{off} (coalescence) and of t_{on}/j_p (refinement) [52]. Consequently, a compromise must be found to obtain the accurate morphology.

In PC, the pulse current density (j_p) is higher than in DC. Consequently, the nucleation rate increases because of the increase of the cathodic overpotential, resulting in a finer morphology for PC coatings. However, the change of t_{off}/j_p or t_{on}/j_p did not have the same impact regarding the nucleation rate. According to Chandrasekar et al. [35], the obtention of fine-grained coatings depends on the one hand on the cathodic reaction occurring during on-times and on the other hand on off-times that encourage the re-nucleation due to the desorption of impurities in the double layer.

In this study, no clear difference in terms of grain size was observed with the change of t_{off}/j_p, which can be explained by the occurrence of different phenomena with antagonist effects on grain size as previously explained.

Fig. 5 clearly shows that the morphology became finer when t_{on} decreased (and j_p increased) at the same t_{off} value of 16 ms. As previously explained, the deposition potential decreased with the increase of j_p (Table 3). In this case, it can be supposed that the overpotential differences were high enough (150 mV between ZnFe14 and ZnFejp125, 160 mV between ZnFejp125 and ZnFejp225 and 1340 mV between ZnFejp225 and ZnFejp1025) to lead to a refinement of the microstructure among PC coatings. Pagotto et al. [39] have also observed finer grains with the decrease of t_{on}, with constant t_{off} in the case of Zn–Ni coatings. In their case, the pulse current density was constant (assuming that the deposition potential was also constant), and the average current density decreased with t_{on}.

It can be concluded from these observations that the use of PC can lead to finer grains. However, this refinement cannot be only explained by overpotential differences. It seems that among PC deposits, some parameters are more influent than others, particularly t_{on}/j_p.

Even though finer grains can present advantages in terms of properties (hardness, corrosion), the t_{on}/t_{off} couple chosen was 4 ms/16 ms, since it was the best to reduce the impact of hydrogen evolution.

3.4. Comparison DC/optimized PC

The use of the optimized conditions in PC (t_{on}/t_{off}: 4 ms/16 ms) reduces the pores number and refines the microstructure as highlighted by surface SEM images. The analysis of the cross-sections of DC (ZnFe14) and PC (ZnFejp125) deposits confirmed these features. Fig. 6 presents the SEM-BSE images of polished cross-sections of Zn–Fe coatings obtained by DC (ZnFe14) and by optimized PC (ZnFejp125).

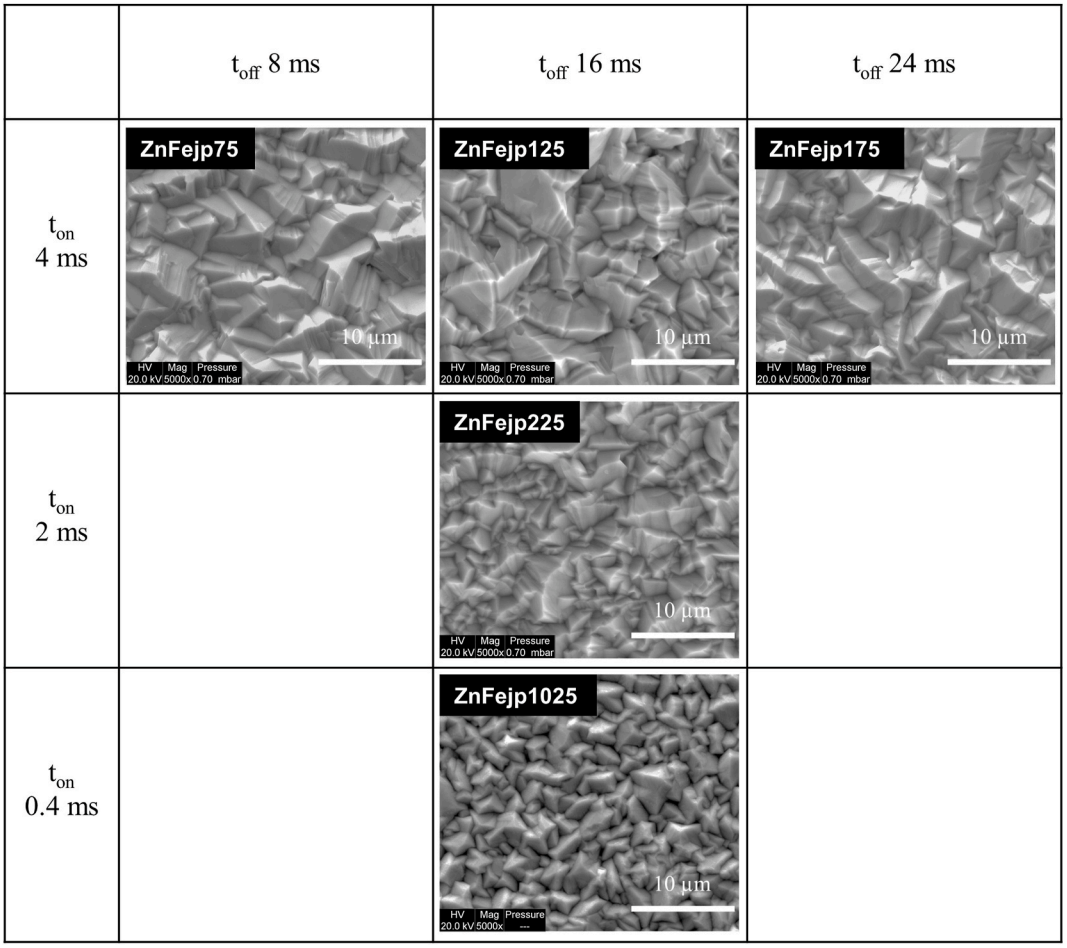

Fig. 5. SEM images (SE) at high magnification (x5000) of the surface of PC deposits obtained at j_m 25 mA/cm^2 on steel substrates, in function of the off-time and the on-time. The pulse current density is given with the name of each specimen.

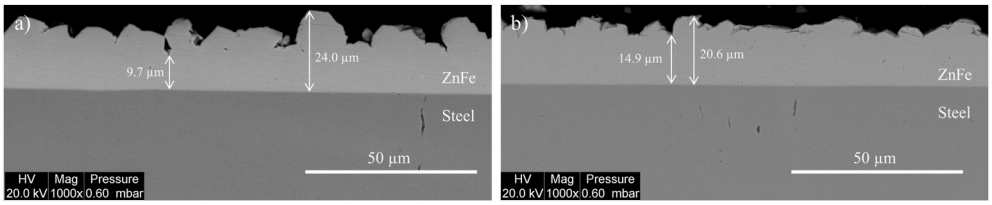

Fig. 6. SEM images (BSE) of polished cross-sections of DC deposit ZnFe14 (a) and PC deposit ZnFejp125 (b). Both deposits were obtained at 25 mA/cm^2 (j or j_m). Deposition parameters for PC deposit were t_{on} 4 ms, t_{off} 16 ms and j_p 125 mA/cm^2.

DC and PC coatings had similar mean thicknesses (17.3 ± 2.6 µm and 16.6 ± 1.2 µm respectively). Because of the coarse pyramidal grains, the thickness of DC coating varied from 9.7 to 24.0 µm while it was in a range from 14.9 to 20.6 µm for PC coating thanks to finer grains, thus reducing the roughness of the deposit. These results confirmed the conclusions of the surface observations: the use of PC leads to a more homogeneous surface with a finer morphology, resulting in smaller pyramidal grains which reduced the standard deviation of the thickness. Since the coatings had similar iron contents, the improvements could be attributed to the use of PC.

Cryogenic fracture was also performed to analyse the cross-section of ZnFejp125. The SEM cross-section is presented in Fig. 7.

The cross-section reveals a columnar morphology of the deposit with a growth direction perpendicular to the substrate. Regarding the width of the columns, it increased from the substrate (eg 1.8 µm) to the surface (eg 5.9 µm). When reaching the surface, the pyramidal shape of the grains is clearly visible, in agreement with the morphology observed on top-view images (Fig. 7). This image also reveals the boundaries between the columns. Most columns are quite closed, particularly near the substrate, which provides the dense aspect of this inner layer. Even though the deposit is quite compact, few columns are less connected, especially near the surface. Since the structure of the deposit is denser near the substrate, it could provide a good barrier against corrosion. The cryofracture highlighted some important characteristics that were erased by the mechanical grinding on polished cross-section. Indeed, the structure of the cross-section can provide some hints regarding the anticorrosion properties.

3.5. Reduction of the iron content

The previous results showed that the current density seems to control the iron content. Nevertheless, in direct mode, dendritic deposits are

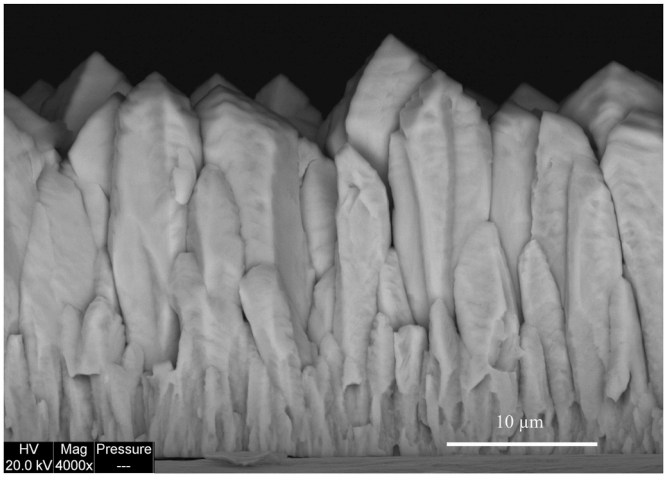

Fig. 7. SEM images (BSE) of the cross-section obtained by cryogenic fracture for ZnFejp125.

obtained when current density is increased to reduce the iron content. Consequently, in order to evaluate the influence of the iron content on the anti-corrosion performance of Zn–Fe alloys, tests were carried out to obtain Zn–Fe deposits with an iron content inferior to 10 wt%. Two ways were investigated: the use of PC with a variation of j_m and the modification of the electrolyte associated to DC.

3.5.1. *Modification of j_m associated to PC*

First, it was decided to use the bath 3 associated to PC to obtain deposits with lower iron content. As showed previously, pulse parameters such as t_{on}, t_{off} and j_p had no effect on the composition of alloys. Thus, a study was performed at constant t_{on} (4 ms) and t_{off} (16 ms). These values were chosen to obtain the optimized properties of the coating. J_p was adapted to vary j_m from 15 to 40 mA/cm^2, as listed in Table 4 and Fig. 8 presents the SEM images of the surface of these deposits at low (x70) and high (×5000) magnifications.

SEM analysis of the surface of ZnFejm40 underlined the dendritic aspect of the coating. Although the use of PC permits to apply higher current densities during very short periods, the j_m value cannot exceed the limiting current density in DC mode.

Fig. 8 shows a change in the morphology among the deposits: ZnFejm15 presents nodular grains while all other deposits are composed of pyramidal grains. The nodular morphology was mentioned for alloys with high iron contents [50]. When j_m increased, the morphology changed to pyramidal, which is the one observed in our case for deposits containing about 14 wt% Fe. Thus, the evolution of the morphology suggests a decrease of the iron content with j_m.

This hypothesis was confirmed by EDS measurements: the iron content decreased with j_m but it remained quite constant for deposits obtained above 25 mA/cm^2. At low j_m, an iron-rich deposit was obtained (about 70 wt%) which is consistent with the observed nodular morphology. The analysis of ZnFejm15 also indicated higher amount of oxygen compared to other coatings (about 5.5 wt%). Other deposits contained less than 20 wt% Fe, which explains their pyramidal grains. ZnFejm20 and ZnFejm22 had higher iron contents compared to ZnFejm25 and ZnFejm30. They also presented finer morphologies. As explained in the part 3.3.2, t_{on} and j_p seem to be the most influent parameters in terms of refinement of the microstructure. However, the on time was the same for all PC deposits and deposits with the highest j_p (ZnFejm25 and ZnFejm30) did not present the finest morphologies. Consequently, the refinement of the microstructure of ZnFejm20 and ZnFejm22 could be attributed to the higher iron content or to a different amount of impurities incorporated compared to ZnFejm25 and ZnFejm30.

SEM images also highlighted a decrease of the pores number when j_m increased, but no increase of the CCE was observed. Once again, j_p increased with j_m and the deposition potential became more negative. Such potentials were usually attributed to the formation of more hydrogen, which was not the case here. Previous results showed that the presence of iron increased the HER. It could be supposed that the decrease of the number of pores with increasing j_m was due to the decrease of the iron content. Such change in hydrogen evolution has been noticed by Nakano et al. [33,34] with the increase of current density. They attributed this phenomenon to the anomalous character of the codeposition.

Fig. 9 is the graph wt.% Fe = f(j) which compares the evolution of the iron content with the applied current density in DC and with j_m in PC. The first evidence is that the same tendency is observed for DC and PC depositions: the iron content is very high at low current densities and it abruptly decreases when the current density increases. Then the iron content remains quite constant over the range 20–30 mA/cm^2 and very close to the composition reference line (CRL). It is in good agreement with a shift from normal codeposition (where the iron content in the alloy is superior to the one in the electrolyte) to anomalous codeposition (where the iron content in the alloy is inferior to the one in the electrolyte). Such evolution has been mentioned in the literature for Zn–Fe zincate and sulfate systems by Nakano et al. [28] and for Zn–Fe acidic chloride system by Jensen et al. [53]. Brenner [30] has also presented this transition for Zn–Ni and Zn–Fe systems, showing that this kind of transition is not always observed depending on the temperature or the composition of the electrolyte. This graph also confirms that in PC, the composition of the alloys seems to be ruled by j_m, but since the change of j_m did not permit to reach iron contents inferior to 10 wt%, the composition of the electrolyte was changed.

Table 4
Elaboration conditions, iron content and deposition potential of PC deposits, with t_{off} 16 ms, t_{on} 4 ms at 25 °C in bath 3 under magnetic stirring (350 rpm).

Name	t_{on} (ms)	t_{off} (ms)	j_p (mA/cm^2)	j_m (mA/cm^2)	%Fe	$E_{deposit}$ (V/SCE)
Zn-Fejm15	4	16	75	15	72.2	−1.71
Zn-Fejm20	4	16	100	20	18.6	−1.74
Zn-Fejm22	4	16	112.5	22.5	17.8	−1.78
Zn-Fejm25	4	16	125	25	14.5	−1.8
Zn-Fejm30	4	16	150	30	15.8	−1.85
Zn-Fejm40	4	16	200	40	12.1	−1.89

3.5.2. *Modification of the electrolyte composition*

In this new electrolyte (bath 4), the iron content was decreased, and the zinc content was increased, as shown in Table 1 in order to increase the Zn/Fe ratio of the coating. Three current densities were tested: 25, 20 and 15 mA/cm^2. The last one was chosen to obtain the accurate iron content for the study. Fig. 10 presents the SEM images of a deposit obtained at 15 mA/cm^2 in DC. The iron content measured by EDS was about 7 wt% and the oxygen content was inferior to 1 wt%, as for most of previous coatings. The CCE calculated was still superior to 90%. The coating presented a homogeneous surface with very few small cavities, due to hydrogen evolution. The reduction of the number of pores could be attributed to the smaller iron content compared to ZnFe14. The alloy was composed of blunted pyramidal grains. No improvement with PC deposition was needed for this deposit.

3.6. *Microstructure*

The crystallographic phases of the three optimized deposits (Zn, ZnFe7 and ZnFejp125) were determined by XRD. Fig. 11 presents the

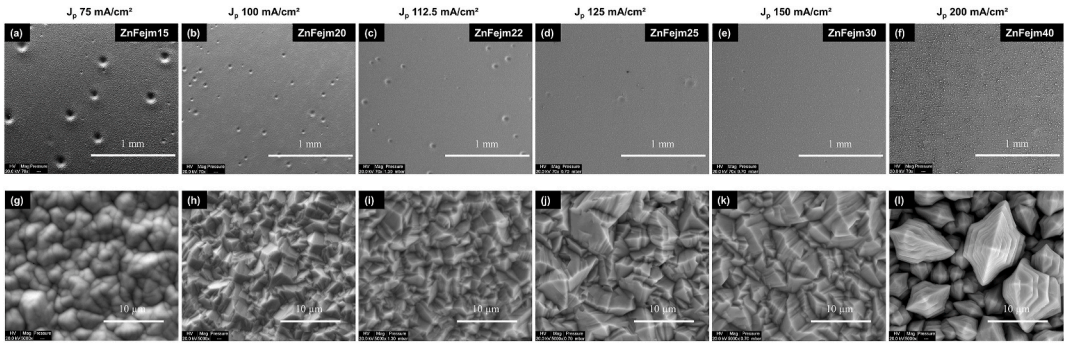

Fig. 8. SEM images (SE) of PC deposits at low (x70) and high (×5000) magnifications: ZnFejm15 (a, g), ZnFejm20 (b, h), ZnFejm22 (c, i), ZnFejm25 (d, j), ZnFejm30 (e, k) and ZnFejm40 (f, l) with iron contents of 72.2, 18.6, 17.8, 14.5, 15.8 and wt.% respectively. All deposits were performed at t_{on} 4 ms and t_{off} 16 ms.

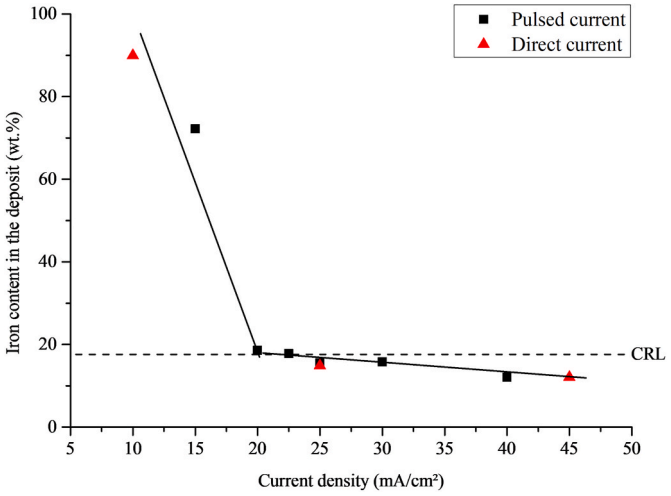

Fig. 9. Evolution of the iron content in DC and PC deposits in function of the applied current density (j_m in the case of PC). The dash-line represents the compositional reference line (CRL), which is the iron content in the electrolyte.

diffractograms of these coatings. Zn deposit was composed of η-Zn phase (h.c.p). Only the most intense peaks were indexed. The diffractogram did not show any preferential orientation for this phase, which is consistent with the random distribution of hexagonal platelets highlighted by SEM observations.

According to the equilibrium diagram, ZnFe7 and ZnFejp125 should be respectively constituted of ζ-$FeZn_{13}$ and δ-$FeZn_{10}$ phases and δ-$FeZn_{10}$ and Γ_1-Fe_5Zn_{21} phases. However, electrodeposits often tend to be composed of metastable phases [31]. For ZnFe7, most peaks were attributed to η and δ phases which is consistent with previous works [9,11,28]. Indeed, η and/or δ were detected for Zn–Fe deposits with the same iron content, with a predominance of η. Even though ζ is present in the equilibrium diagram, it has scarcely been detected for zinc-iron electrodeposits [22,27,40].

Previous works highlighted the presence of η and/or δ and/or Γ_1 phases for coatings with about 14 wt% Fe [8,9,11]. According to Hara et al. [54], δ was supposed to be the main phase in such electrodeposit.

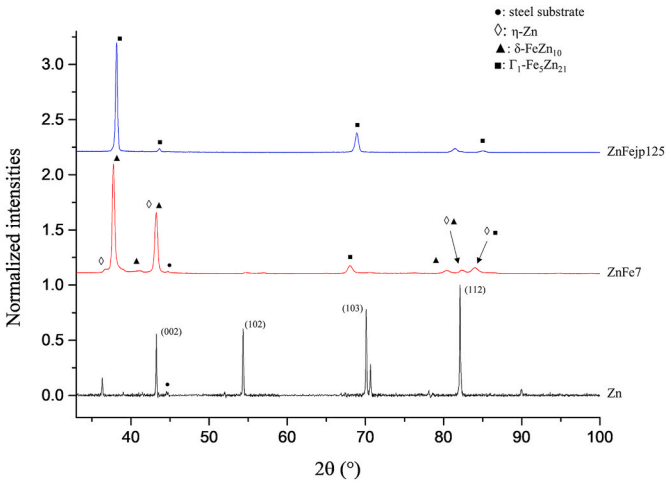

Fig. 11. Diffractograms of optimized coatings Zn, ZnFe7 (7 wt% Fe) and ZnFejp125 (14.5 wt% Fe).

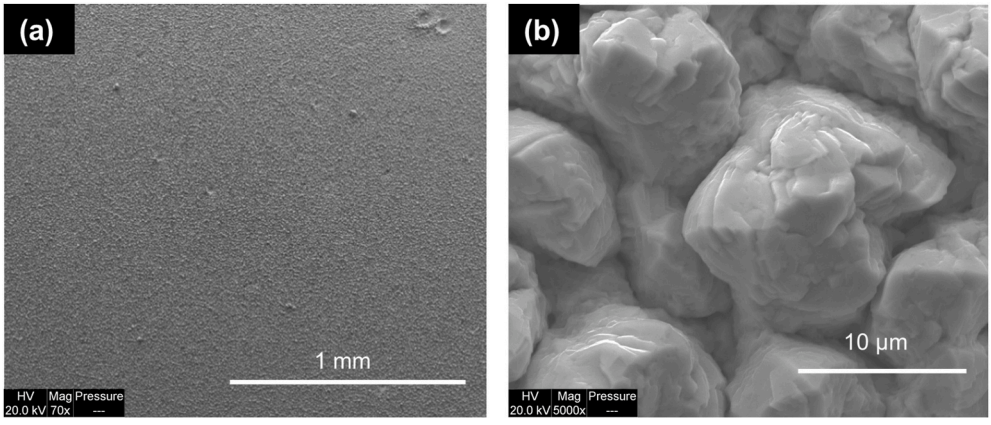

Fig. 10. SEM images (SE) of the surface of ZnFe7 DC electrodeposit obtained at 15 mA/cm^2, with a low iron content (about 7 wt% Fe) at low (x70) (a) and high (×5000) (b) magnifications.

Moreover, authors have noted the formation of Γ-Fe_3Zn_{10} (b.c.c) and Γ_1-Fe_5Zn_{21} (f.c.c) phases when the amount of iron in the alloy increases. Kondo et al. [8] have attributed the formation of pyramidal grains to the presence of these two cubic phases. Thus, the pyramidal shape of ZnFejp125 associated to the XRD observations suggests that Γ_1 is the main phase in this deposit.

Table 5 summarizes the differences between the expected crystallographic phases according to the equilibrium diagram and to the literature in comparison with the detected crystallographic phases, for ZnFe7 and ZnFejp125. The presence of the solid solution η at such iron contents (about 7 and 14 wt%) is not in agreement with the equilibrium diagram but it has been widely mentioned in the literature [8,9,11,13,16,27,28,42,43]. Indeed, authors have noticed an enlargement of the stability range of terminal solid solutions (such as η) for electrodeposited coatings [31]. These results confirmed the fact that electrodeposited zinc-iron coatings have metastable structures. The disparities in terms of microstructure are well known and are explained by several factors. The identification of Zn–Fe crystallographic phases is complicated since some of them can coexist in the alloy. Moreover, the structure of the deposits is greatly dependent on the electrolyte and on the deposition conditions.

The functional properties of three deposits (Zn, ZnFe7 and ZnFejp125) are now evaluated to determine the influence of the iron content and the phase composition.

3.7. Micro-indentation and scratch-tests

The micro-hardness values calculated from equation (4) are gathered in Table 6. The applied load was adjusted in order to minimize the substrate influence on the hardness values and to limit the penetration depth [46]. The steel substrate is received in an annealed state corresponding to a ferrite-perlitic structure, which is consistent with the micro-hardness value around 332 $HV_{0.01}$. The electrodeposited zinc coating presents a very low micro-hardness value of 53 $HV_{0.01}$. This value is consistent with those reported in the literature for pure electroplated zinc coatings [55,56]. Incorporation of iron markedly increases the micro-hardness of zinc-based coatings. Rashmi et al. [57] also reported an increase for Zn–Fe coatings (2–5 wt%) deposited from an acidic bath, with values ranging from 120 up to 180 HV according to the deposition process. Panagopoulos et al. [11] noticed the same tendency regarding micro-hardness (from 56 HV for Zn to 203 HV for 14 wt % Fe Zn–Fe). ZnFe7 coating (7 wt% Fe) has an average micro-hardness of 258 $HV_{0.01}$, whereas ZnFejp125 (14 wt% Fe) does not present an important additional hardness increase, reaching an average value of 292 $HV_{0.01}$. The electrodeposited ZnFe7 is composed of a mixture of pure η-Zn and δ-$ZnFe_{10}$ phases whereas ZnFejp125 seems to be mainly composed of the Γ_1-Zn_5Fe_{21} phase. Inui et al. [58] have studied the mechanical properties of the Zn–Fe intermetallic phases through a compression test performed on specimens obtained by FIB from galvanized coatings. They noticed a micro-hardness increase with iron incorporation, but they reported plastic deformation on ζ-$FeZn_{13}$, δ-$FeZn_{10}$ and Γ phases whereas Γ_1-Zn_5Fe_{21} phase was brittle. The hardness values of δ and Γ_1 phases were reported at around 380 and superior to 500 HV respectively. The presence of δ phase in the dual-phase electrodeposited ZnFe7 coating could explain the hardness increase compared to that of pure zinc. According to XRD analysis, ZnFejp125 is only composed of Γ_1 phase. However, the hardness of the coating is inferior to the values reported for this crystallographic phase. ZnFejp125 cross-section (figure) highlighted the columnar growth of the coating. Nanopores could appear during the formation and the growth of the columns. The presence of these nanopores at the junction of the columns could explain the unexpected low hardness of ZnFejp125 compared to that of Γ_1 phase.

Table 5
Comparison of the phase composition of DC ZnFe7 (about 7 wt% Fe) and optimized PC ZnFejp125 (about 14 wt% Fe).

		Phase composition according to		
Deposit	Wt.% Fe	Equilibrium diagram	Literature	This study
ZnFe7	7.5	ζ + δ	η/δ	η + δ
ZnFejp125	14.5	δ + Γ_1	η/δ/(Γ_1/Γ)	Γ_1

Table 6
Comparison of micro-hardness and penetration depth measured for steel substrate and optimized zinc-based electrodeposits.

Sample	36NiCrMo16	Zn	ZnFe7	ZnFejp125
Iron content (wt.%)	–	0	7	14
Micro-hardness $HV_{0.01}$	332 ± 8	53 ± 4	258 ± 17	292 ± 31
Penetration depth (μm)	1.1 ± 0.1	2.8 ± 0.3	1.8 ± 0.4	1.3 ± 0.1

Scratch test is not very used for assessing adhesion of soft coatings. However, the examination of the tracks or of the residual depth [59] permits to determine critical loads corresponding to the different damages of the coatings. Fig. 12 presents the optical observations of the tracks after the scratch test on the different zinc-based coatings. The scratch behaviours of both pure zinc and ZnFe7 coatings are quite similar. These coatings present important plastic deformations without formation of cracks during the test.

Pure zinc coating (53 $HV_{0.01}$) presents a very important plastic deformation that limits the tip penetration and the plastic deformation of the substrate. It is not possible to determine the critical load that may correspond to the wiping of the coating inside the track. It means that the use of a larger force is required to remove completely the coating from the scratch tracks. It is reported that such critical load is around 9.7 N for a 10 μm thick zinc coated steel or 38.5 N for a 5 μm pure zinc layer obtained by PVD [60,61]. The present study highlighted a residual penetration of the indenter at the highest load (5 N) of approximately 10 μm for the zinc coating, corresponding to the thickness of the layer.

The scratch behaviour is quite similar between pure zinc and ZnFe7 (7 wt% Fe) coatings, perhaps in relation with the predominance of η-Zn rich phase. Even if the micro-hardness value is close to 257 $HV_{0.01}$, the ZnFe7 coating presents the same aptitude to limit the tip penetration due to plastic deformation. Effectively, the residual indenter penetration is also quite similar to that of pure zinc, with a maximum around 10 μm. But, contrary to pure zinc, chipping is observed for a critical load of 3.5 N (Fig. 12) corresponding to a cohesive failure in the coating due to the high plastic deformation.

ZnFejp125 (14 wt% Fe) presents a quite different behaviour, even though its hardness is not so different from ZnFe7. Chipping is detected for a lower critical load of 1.5 N, due to the fact that plastic deformation is less important. Winiarski [62] observed three critical loads during the scratch-test of a ternary electrodeposited Zn–Fe–Mo coating, and the first one corresponds to the cohesive cracks in the coating for values ranging from 1.5 to 2.2 N. The indenter penetration of approximately 40 μm is noticed for the coating with 14 wt% Fe.

A brittle behaviour is noticed with the formation of local cracks and spallation. At a normal load of about 4 N, the tip reaches the substrate. The steel substrate underwent a plastic deformation and material raised at the edges of the scratches which explains the high residual penetration values observed for the latest coating.

The comparison of the tracks in Fig. 12 permits to conclude that pure zinc and low iron content zinc alloy present good adhesion onto the steel substrate. The high plastic deformation of these coatings limits the depth penetration of the tip and the coatings are not removed from the steel substrate. Regarding 14 wt% Fe coatings, the more brittle behaviour leads to high abrasion and scribes away the film, resulting in a clear scratch and visible substrate. This brittle behaviour is probably linked to microstructural evolution and particularly to the presence of Γ_1. So, the adhesion strength seems to be reduced for the high iron amount.

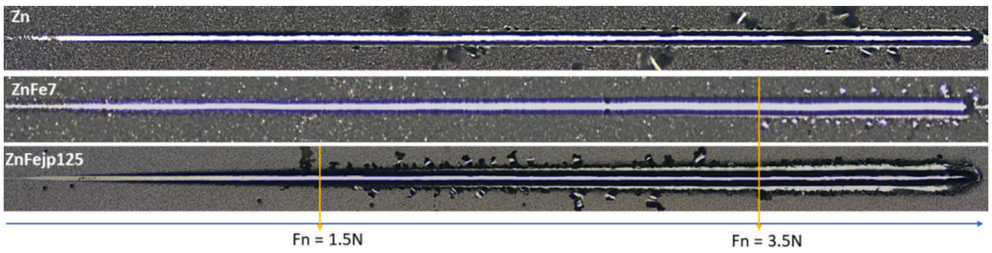

Fig. 12. Scratch tracks obtained for optimized coatings deposited on steel substrates: Zn, ZnFe7 and ZnFejp125.

3.8. Corrosion of the optimized coatings

The polarization curves after 1h of immersion in 3.5 wt% NaCl solution of the steel substrate and the Zn-based coatings are presented in Fig. 13. All coatings have corrosion potentials less noble than the one of steel, highlighting their sacrificial behaviour. The objective of adding iron to zinc coatings is to shift their corrosion potential towards the one of steel, thus limiting the galvanic coupling between them. Table 7 presents the corrosion potentials (E_{corr}) and current densities (j_{corr}) of the different samples. As expected, the corrosion potential of ZnFejp125 is between the one of Zn and the one of steel. However, no significant change of corrosion potential was observed between Zn and ZnFe7 coatings. It seems that there is a threshold value of the iron content: below this value there is no effect of iron on the corrosion potential of the coating. This hypothesis could be explained by the microstructure of the deposits. As shown in part 3.6, η and δ were detected for ZnFe7. A high amount of η phase in ZnFe7 could explain the fact that it has the same corrosion potential as Zn, showing the correlation between the metallurgical features and the functional properties of the coating. There is a slight decrease of the corrosion current density when iron is added to zinc coating, but no difference is noted between ZnFe7 and ZnFejp125.

Consequently, ZnFejp125 seems the most promising solution in terms of corrosion resistance because of the increase of its corrosion potential, which may be related to the presence of only Γ_1 phase.

4. Conclusion

Zn and Zn–Fe alloys with 7 and 14 wt% Fe were obtained with an additive-free electrolyte composed of potassium hydroxide, zinc oxide and ferrous gluconate. Homogeneous Zn and Zn–Fe 7 wt% Fe were obtained by direct current plating. However, a further increase of the iron content in the coating up to 14 wt% favored the HER, leading to the presence of many pores due to hydrogen formation. Instead of adding additives in the electrolyte, pulse current mode was used to reduce the impact of HER. The impact of pulse parameters on the metallurgical features of a high iron content deposit (14 wt%) was investigated. The modification of t_{on}, t_{off} and j_p played a marked role only on the morphology of the deposits, by reducing the number of pores and forming finer grains, thus reducing the roughness of the coating. The modification of j_m was found to control the iron content of electrodeposits. However, the same tendency and values were observed for DC and PC deposits, without changing the normal/anomalous codeposition transition that could be observed for Zn-M systems, where M is an iron-group metal. The determination of crystallographic phases highlighted the presence of η for Zn, and of η, δ for ZnFe7, and Γ_1 for ZnFejp125. Iron incorporation led to an increase of the coating micro-hardness. The evolution of the metallurgical state with iron incorporation, particularly in terms of phase composition, also affected the micro-hardness, justifying the very low difference of hardness between the 7 wt% Fe and 14 wt% Fe alloys. The high plastic deformation of the low iron content alloy and pure zinc limited the coating abrasion suggesting a very good adhesion of the coatings. The more brittle behaviour of the 14 wt% Zn–Fe alloy reduced its adhesion strength onto the steel substrate. Polarization curves in 3.5 wt% NaCl highlighted the sacrificial behaviour of all coatings. Adding 7 wt% of iron to zinc was not enough to increase its corrosion potential. This observation was associated to the similarities of microstructure between ZnFe7 and Zn. For the ZnFejp125, the corrosion potential was significantly increased, and this deposit seemed promising regarding corrosion resistance.

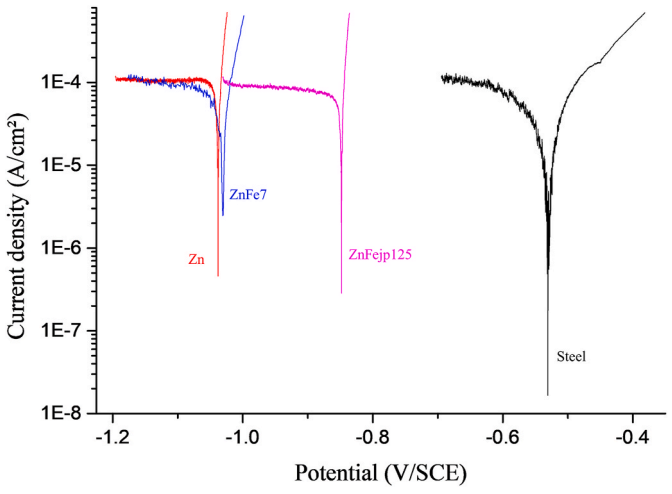

Fig. 13. Polarization curves of steel and optimized coatings Zn, ZnFe7 (7 wt% Fe) and ZnFejp125 (14.5 wt% Fe) obtained in aerated 3.5 wt% NaCl under magnetic stirring (250 rpm) after 1 h at OCP.

Table 7
Corrosion potential (E_{corr}) and current densities (j_{corr}) of the steel substrate and the optimized Zn-based coatings (7 wt% Fe for ZnFe7, 14.5 wt% Fe for ZnFejp125). Corrosion characteristics obtained during polarization curves after 1h of OCP in 3.5 wt% NaCl, pH 7, at 25 °C under magnetic stirring (250 rpm).

Sample	E_{corr} (V/SCE)	j_{corr} (μA/cm^2)
Steel	−0.528	60
Zn	−1.037	105
ZnFe7	−1.029	76
ZnFejp125	−0.847	73

CRediT authorship contribution statement

C. Arrighi: Writing - original draft, Investigation, Writing - review & editing. **C. Savall:** Supervision, Writing - review & editing. **S. Cohendoz:** Investigation. **J.-L. Grosseau-Poussard:** Investigation. **L. Baissac:** Investigation. **M.-G. Olivier:** Funding acquisition, Supervision, Writing - review & editing. **J. Creus:** Funding acquisition, Supervision, Writing - review & editing.

Declaration of competing interest

The authors declare that they have no known competing financial interests or personal relationships that could have appeared to influence

the work reported in this paper.

Acknowledgement

This study was co-supported by the Nouvelle Aquitaine Region in France and the University of Mons in Belgium through the Project Dursadh: 2017-1R10101. The authors thank particularly C. Rébéré, E. Conforto and G. Lotte for their contributions for the metallurgical characterization of the electrodeposited coatings.

References

[1] K.R. Baldwin, C.J.E. Smith, Advances in replacements for cadmium plating in aerospace applications, Trans. Inst. Met. Finish. 74 (1996) 202–209, https://doi.org/10.1080/00202967.1996.11871127.
[2] G.D. Wilcox, D.R. Gabe, Electrodeposited zinc alloy coatings, Corrosion Sci. 35 (1993) 1251–1258, https://doi.org/10.1016/0010-938X(93)90345-H.
[3] R. Ramanauskas, P. Quintana, L. Maldonado, R. Pomés, M.A. Pech-Canul, Corrosion resistance and microstructure of electrodeposited Zn and Zn alloy coatings, Surf. Coating. Technol. 92 (1997) 16–21, https://doi.org/10.1016/S0257-8972(96)03125-8.
[4] K.R. Baldwin, M.J. Robinson, C.J.E. Smith, The corrosion resistance of electrodeposited zinc-nickel alloy coatings, Corrosion Sci. 35 (1993) 1267–1272, https://doi.org/10.1016/0010-938X(93)90347-J.
[5] Z. Feng, Q. Li, J. Zhang, P. Yang, H. Song, M. An, Electrodeposition of nanocrystalline Zn-Ni coatings with single gamma phase from an alkaline bath, Surf. Coating. Technol. 270 (2015) 47–56, https://doi.org/10.1016/j.surfcoat.2015.03.020.
[6] M.H. Sohi, M. Jalali, Study of the corrosion properties of zinc-nickel alloy electrodeposits before and after chromating, J. Mater. Process. Technol. 138 (2003) 63–66, https://doi.org/10.1016/S0924-0136(03)00050-5.
[7] I.H. Karahan, Effects of pH value of the electrolyte and glycine additive on formation and properties of electrodeposited Zn-Fe coatings, Sci. World J. 2013 (2013), https://doi.org/10.1155/2013/273953. Article ID 273953, 7 pages.
[8] K. Kondo, S. Hinotani, Y. Ohmori, Crystal structure and morphology of electrodeposited zinc-iron binary alloys, J. Appl. Electrochem. 18 (1988) 154–161, https://doi.org/10.1007/BF01016220.
[9] K. De Wit, A. De Boeck, B.C. De Cooman, Study of the influence of phase composition and iron content on the formability characteristics of zinc-iron electroplated sheet steel, J. Mater. Eng. Perform. 8 (1999) 531–537, https://doi.org/10.1007/s11665-999-0005-7.
[10] C.N. Panagopoulos, P.E. Agathocleous, V.D. Papachristos, A. Michaelides, Sliding wear behaviour of zinc-iron alloy electrodeposits, Surf. Coating. Technol. 123 (2000) 62–71, https://doi.org/10.1016/j.jmatprotec.2004.06.014.
[11] C.N. Panagopoulos, E.P. Georgiou, P.E. Agathocleous, K.I. Giannakopoulos, Mechanical behaviour of Zn-Fe alloy coated mild steel, Mater. Des. 30 (2009) 4267–4272, https://doi.org/10.1016/j.matdes.2009.04.026.
[12] H. Park, J.A. Szpunar, The role of texture and morphology in optimizing the corrosion resistance of zinc-based electrogalvanized coatings, Corrosion Sci. 40 (1998) 525–545, https://doi.org/10.1016/S0010-938X(97)00148-0.
[13] K.O. Nayana, T.V. Venkatesha, K.G. Chandrappa, Influence of additive on nanocrystalline, bright Zn-Fe alloy electrodeposition and its properties, Surf. Coating. Technol. 235 (2013) 461–468, https://doi.org/10.1016/j.surfcoat.2013.08.003.
[14] M. Kanagasabapathy, S. Jayakrishnan, Textural and morphological studies on zinc-iron alloy electrodeposits, J. Chem. Sci. 123 (2011) 357–364, https://doi.org/10.1007/s12039-011-0074-7.
[15] J.B. Bajat, V.B. Mišković-Stanković, M.D. Maksimović, D.M. Dražić, S. Zec, Electrochemical deposition and characterization of Zn-Fe alloys, J. Serb. Chem. Soc. 69 (2004) 807–815, https://doi.org/10.2298/JSC0410807B.
[16] C.A. Drewien, J.I. Goldstein, A.R. Marder, Structure of as-deposited iron-zinc coatings from chloride bath, Metall. Mater. Trans. 25 (1994) 249–255, https://doi.org/10.1007/BF02647970.
[17] V. Thangaraj, Electrodeposition and corrosion behaviour of some Zn-Fe group metal alloys by pulsed current, Trans. Inst. Met. Finish. 87 (2009) 208–216, https://doi.org/10.1179/174591909X424816.
[18] A.C. Hegde, K. Venkatakrishna, N. Eliaz, Electrodeposition of Zn-Ni, Zn-Fe and Zn-Ni-Fe alloys, Surf. Coating. Technol. 205 (2010) 2031–2041, https://doi.org/10.1016/j.surfcoat.2010.08.102.
[19] S. Amirat, R. Rehamnia, M. Bordes, J. Creus, Zn-Fe alloy electrodeposition from chloride bath: influence of deposition parameters on coatings morphology and structure, Mater. Corros. 64 (2013) 328–334, https://doi.org/10.1002/maco.201106290.
[20] C.-C. Hu, A. Bai, The inhibition of anomalous codeposition of iron-group Alloys using cyclic voltammetry, J. Electrochem. Soc. 149 (2002), https://doi.org/10.1149/1.1511753. C615.
[21] H.L. Hu, Y.M. Zhu, Z.M. Tu, W.J. Liu, High anticorrosion nano Zn-Fe coatings by pulse electrodepositing, Adv. Mater. Res. 194–196 (2011) 2209–2215. https://doi.org/10.4028/www.scientific.net/AMR.194-196.2209.
[22] I.H. Karahan, H.A. Çetinkara, H.S. Güder, Electrodeposition and characterisation of Zn, Zn-Fe and Zn-Fe-Ni coatings in presence of gelatin as additive, Trans. Inst. Met. Finish. 86 (2008) 157–161, https://doi.org/10.1179/174591908X304171.
[23] Z.N. Yang, Z. Zhang, J.Q. Zhang, Electrodeposition of decorative and protective Zn-Fe coating onto low-carbon steel substrate, Surf. Coating. Technol. 200 (2006) 4810–4815, https://doi.org/10.1016/j.surfcoat.2005.04.026.
[24] L.L. Barbosa, G.A. Finazzi, P.C. Tulio, I.A. Carlos, Electrodeposition of zinc-iron alloy from an alkaline bath in the presence of sorbitol, J. Appl. Electrochem. 38 (2008) 115–125, https://doi.org/10.1007/s10800-007-9409-y.
[25] Y. Wang, H. Xiao, L. Chai, Current efficiency improvement of Zn-Fe alloy electrodeposition by hydrogen inhibitor, J. Cent. South Univ. Technol. 15 (2008) 814–818, https://doi.org/10.1007/s11771-008-0150-4.
[26] A. Roshanghias, M. Heydarzadeh Sohi, The effects of pulse plating variables on morphology and corrosion behavior of Zn-Fe alloy coatings, J. Coating Technol. Res. 9 (2012) 215–218, https://doi.org/10.1007/s11998-010-9249-2.
[27] C.J. Lan, W.Y. Liu, S.T. Ke, T.S. Chin, Potassium salt based alkaline bath for deposition of Zn-Fe alloys, Surf. Coating. Technol. 201 (2006) 3103–3108, https://doi.org/10.1016/j.surfcoat.2006.06.027.
[28] H. Nakano, S. Arakawa, S. Oue, S. Kobayashi, Electrodeposition behavior of ZnFe alloy from zincate solution containing triethanolamine, Mater. Trans. 56 (2015) 1664–1669, https://doi.org/10.2320/matertrans.M2015230.
[29] C.J. Lan, W.Y. Liu, T.S. Chin, Electrodeposition of Zn–Fe alloys using electrolytes of the system ZnO–(ferrous gluconate)–KOH, J. Electrochem. Soc. 154 (2007), https://doi.org/10.1149/1.2393011. D30.
[30] A. Brenner, Electrodeposition of alloys containing an iron-group metal and zinc or cadmium, Electrodepos. Alloy (1963) 194–238, https://doi.org/10.1016/b978-1-4831-9807-1.50020-9.
[31] Y.D. Gamburg, G. Zangari, Theory and Practice of Metal Electrodeposition, Springer Science, business media, 2011, https://doi.org/10.1007/978-1-4419-9669-5.
[32] K.I. Popov, S.S. Djokic, B.N. Grgur, Fundamental Aspects of Electrometallurgy, Springer US, 2002, https://doi.org/10.1007/b118178.
[33] H. Nakano, S. Arakawa, S. Oue, S. Kobayashi, Electrodeposition behavior of Zn-Ni alloys from an alkaline zincate solution containing ethylenediamine, ISIJ Int. 53 (2013) 1864–1870, https://doi.org/10.2355/isijinternational.53.1864.
[34] H. Nakano, S. Shibata, S. Arakawa, S. Oue, S. Kobayashi, Electrodeposition behavior of Zn-Co alloys from zincate solution containing triethanolamine, ISIJ Int. 53 (2013) 1858–1863, https://doi.org/10.2320/jinstmet.J2014054.
[35] M.S. Chandrasekar, M. Pushpavanam, Pulse and pulse reverse plating-Conceptual, advantages and applications, Electrochim. Acta 53 (2008) 3313–3322, https://doi.org/10.1016/j.electacta.2007.11.054.
[36] R. Ramanauskas, L. Gudavičiute, R. Juškenas, O. Ščit, Structural and corrosion characterization of pulse plated nanocrystalline zinc coatings, Electrochim. Acta 53 (2007) 1801–1810, https://doi.org/10.1016/j.electacta.2007.08.036.
[37] Y. Boonyongmaneerat, S. Saenapitak, K. Saengkiettiyut, Reverse pulse electrodeposition of Zn-Ni alloys from a chloride bath, J. Alloys Compd. 487 (2009) 479–482, https://doi.org/10.1016/j.jallcom.2009.07.163.
[38] Y. Boonyongmaneerat, K. Saengkiettiyut, S. Saenapitak, S. Sangsuk, Corrosion behavior of reverse-pulse electrodeposited Zn-Ni alloys in saline environment, J. Mater. Eng. Perform. 23 (2014) 302–307, https://doi.org/10.1007/s11665-013-0685-x.
[39] S.O. Pagotto, C.M. De Alvarenga Freire, M. Ballester, Zn-Ni alloy deposits obtained by continuous and pulsed electrodeposition processes, Surf. Coating. Technol. 122 (1999) 10–13, https://doi.org/10.1016/S0257-8972(99)00401-6.
[40] F.Y. Ge, S.K. Xu, S.B. Yao, S.M. Zhou, Study of the structures of pulse plating Zn-Fe deposits, Surf. Coating. Technol. 88 (1997) 1–4, https://doi.org/10.1016/S0257-8972(96)02922-2.
[41] A.R. Marder, The metallurgy of zinc-coated steel, Prog. Mater. Sci. 45 (2000) 191–271, https://doi.org/10.1016/S0079-6425(98)00006-1.
[42] E. Gómez, E. Pelaez, E. Vallés, Electrodeposition of zinc+iron alloys, J. Electroanal. Chem. 469 (1999) 139–149, https://doi.org/10.1016/S0022-0728(99)00196-5.
[43] G.U. Mingyuan, M.R. Notis, A.R. Marder, The effect of continuous heating on the phase transformations in zinc- iron electrodeposited coatings, Metall. Trans. A. 22 (1991) 1737–1743, https://doi.org/10.1007/BF02646497.
[44] R. Ramanauskas, L. Gudavičiūtė, O. Ščit, Effect of pulse plating on the composition and corrosion properties of Zn – Co and Zn – Fe alloy coatings, Trans. Inst. Met. Finish. 19 (2008) 7–13, https://doi.org/10.1179/174591908X272924.
[45] R.S. Bhat, A.C. Hegde, Electroplating and corrosion study of Zn-Co, Zn-Fe and Zn-Co-Fe alloys, Anal. Bioanal. Electrochem. 4 (2012) 593–609.
[46] A. Iost, G. Guillemot, Y. Rudermann, M. Bigerelle, A comparison of models for predicting the true hardness of thin films, Thin Solid Films 524 (2012) 229–237, https://doi.org/10.1016/j.tsf.2012.10.017.
[47] A.B. Maity, M. Basu, S. Chaudhuri, A.K. Pal, Stress and microhardness in poly crystal line thin films from below-band-gap absorption studies, J. Phys. D Appl. Phys. 28 (1995) 2547–2553, https://doi.org/10.1088/0022-3727/28/12/024.
[48] A. Lasia, Hydrogen Evolution Reaction, Handbook Fuel Cells, John Wiley & Sons, 2010, https://doi.org/10.1002/9780470974001.f204033.
[49] L. Exbrayat, E. Calvié, T. Douillard, G. Marcos, C. Savall, C. Berziou, J. Creus, P. Steyer, Role of ceria nanoparticles on the electrodeposition zinc coatings growth : interest of a TEM-Scale investigation, ECS Electrochem. Lett. 39 (2014) D33–D35, https://doi.org/10.1149/2.0011410eel.
[50] J.-F. Huang, I.-W. Sun, Nonanomalous electrodeposition of zinc-iron alloys in an acidic zinc chloride-1-ethyl-3-methylimidazolium chloride ionic liquid, J. Electrochem. Soc. 151 (2004), https://doi.org/10.1149/1.1628235. C8.
[51] T. Pearson, J.K. Dennis, Facts and Fiction about pluse plating, Trans. Inst. Met. Finish. 69 (1991) 75–79, https://doi.org/10.1080/00202967.1991.11870897.
[52] H. Natter, R. Hempelmann, Tailor-made nanomaterials designed by electrochemical methods, Electrochim. Acta 49 (2003) 51–61, https://doi.org/10.1016/j.electacta.2003.04.004.

[53] J.D. Jensen, G.W. Critchlow, D.R. Gabe, A study on zinc-iron alloy electrodeposition from a chloride-electrolyte, Trans. Inst. Met. Finish. 76 (1998) 187–191, https://doi.org/10.1080/00202967.1998.11871221.
[54] T. Hara, T. Adaniya, M. Sagiyama, T. Honma, A. Tonouchi, T. Watanabe, M. Ohmura, The phase composition and workability of electrodeposited Fe-Zn alloy, Trans. ISIJ. 23 (1983) 954–958, https://doi.org/10.2355/isijinternational1966.23.954.
[55] L. Exbrayat, P. Steyer, C. Rébéré, C. Berziou, C. Savall, P. Ayrault, E. Tertre, G. L. Joly-Pottuz, J. Creus, Electrodeposition of zinc-ceria nanocomposite coatings in alkaline bath, J. Solid State Electrochem. 18 (2014) 223–233, https://doi.org/10.1007/s10008-013-2264-3.
[56] J. Sheng, X. Shen, Y. Wang, Q. Xu, X. Zhang, Microstructure and corrosion behavior of electrodeposited Zn-TiN composite coatings, Mater. Corros. 70 (2019) 1044–1055, https://doi.org/10.1002/maco.201810576.
[57] D. Rashmi, G.P. Pavithra, B.M. Praveen, D. Devapal, K.O. Nayana, S.P. Hebbar, Characterization and corrosion analysis of electrodeposited nanostructured Zn–Fe alloy coatings, J. Bio- Tribo-Corrosion. 6 (2020) 1–8, https://doi.org/10.1007/s40735-020-00380-9.
[58] H. Inui, N.L. Okamoto, S. Yamaguchi, Crystal structures and mechanical properties of Fe-Zn intermetallic compounds formed in the coating layer of galvannealed steels, ISIJ Int. 58 (2018) 1550–1561, https://doi.org/10.2355/isijinternational.ISIJINT-2018-066.
[59] S.J. Bull, E.G. Berasetegui, An overview of the potential of quantitative coating adhesion measurement by scratch testing, Tribol. Int. 39 (2006) 99–114, https://doi.org/10.1016/j.triboint.2005.04.013.
[60] P. Suresh Kuiry, Advanced Scratch Testing for Evaluation of Coatings, Bruker, 2012. https://www.bruker.com/fileadmin/user_upload/8-PDF-Docs/SurfaceAnalysis/TMT/Webinars/Advanced-Scratch-Testing-for-Evaluation-of-Coatings-Slides.pdf.
[61] S. Sabooni, E. Galinmoghaddam, M. Ahmadi, R.J. Westerwaal, J. van de Langkruis, E. Zoestbergen, J.T.M. De Hosson, Y.T. Pei, Microstructure and adhesion strength quantification of PVD bi-layered ZnMg-Zn coatings on DP800 steel, Surf. Coating. Technol. 359 (2019) 227–238, https://doi.org/10.1016/j.surfcoat.2018.12.064.
[62] J. Winiarski, The effect of current density on the structure and mechanical properties of protective Zn–Fe–Mo alloy coatings electrodeposited on a mild steel, Mater. Chem. Phys. 239 (2020), 122258, https://doi.org/10.1016/j.matchemphys.2019.122258.